

# Shadowing Effects on the Nuclear Suppression Factor, $R_{d\text{Au}}$ , in d+Au Interactions

R. Vogt

*Nuclear Science Division, Lawrence Berkeley National Laboratory, Berkeley, CA 94720, USA*

*and*

*Physics Department, University of California, Davis, CA 95616, USA*

## Abstract

We explore how nuclear modifications to the nucleon parton distributions affect production of high transverse momentum hadrons in deuteron-nucleus collisions. We calculate the charged hadron spectra to leading order using standard fragmentation functions and shadowing parameterizations. We obtain the d+Au to  $pp$  ratio both in minimum bias collisions and as a function of centrality. The minimum bias results agree reasonably well with the BRAHMS data while the calculated centrality dependence underestimates the data and is a stronger function of  $p_T$  than the data indicate.

One of the most intriguing results from the Relativistic Heavy Ion Collider (RHIC) at Brookhaven National Laboratory has been the suppression of hadrons with high transverse momentum,  $p_T$ , in central Au+Au collisions at center-of-mass energies,  $\sqrt{S_{NN}}$ , of 130 and 200 GeV. The  $AA$  suppression factor,

$$R_{AA}(p_T) = \frac{d\sigma_{AA}/dp_T}{\langle \sigma_{NN}^{\text{in}} T_{AA} \rangle d\sigma_{pp}/dp_T} , \quad (1)$$

compares the  $AA$  and  $pp$   $p_T$  distributions of hadrons, normalized by the number of binary collisions,  $\langle \sigma_{NN}^{\text{in}} T_{AA} \rangle$ , the product of the nucleon-nucleon inelastic cross section,  $\sigma_{NN}$ , and the nuclear overlap function  $T_{AA}$ . Saturation effects in the initial nuclear wave function and final-state parton energy loss were both proposed as explanations of the large suppression seen in Au+Au collisions by PHENIX [1,2], STAR [3,4] and BRAHMS [5]. To determine whether the suppression is an initial or final-state effect, d+Au collisions at  $\sqrt{S_{NN}} = 200$  GeV were recently studied at RHIC. The data [6–8] show that, at midrapidity ( $\eta \approx 0$ ), the d+Au suppression factor,

$$R_{\text{dAu}}(p_T) = \frac{d\sigma_{\text{dAu}}/dp_T}{\langle \sigma_{NN}^{\text{in}} T_{\text{dAu}} \rangle d\sigma_{pp}/dp_T} , \quad (2)$$

is much closer to unity. These results suggest that the strong suppression in Au+Au collisions is a final-state effect, implying that, at least at central rapidities, saturation effects are small. However, at higher rapidities where the nuclear parton momentum fraction,  $x_2$ , is smaller, such effects might still be important. Since  $x$  is not very small at RHIC, it is necessary to check if other, more conventional, models of nuclear shadowing may also explain the data.

The BRAHMS collaboration has measured  $R_{\text{dAu}}$  at several values of pseudorapidity,  $\eta$ , and observed increasing suppression as  $\eta$  increases from  $|\eta| \leq 0.2$  to  $\eta = 3.2$  [8]. The BRAHMS measurements are in four  $\eta$  bins:  $|\eta| \leq 0.2$ ;  $0.8 \leq \eta \leq 1.2$  ( $\eta = 1$ );  $1.9 \leq \eta \leq 2.35$  ( $\eta = 2$ ) and  $2.9 \leq \eta \leq 3.5$  ( $\eta = 3.2$ ), corresponding to center-of-mass scattering angles,  $\theta_{\text{cm}}$ , of  $101.4^\circ \leq \theta_{\text{cm}} \leq 78.6^\circ$ ,  $48.4^\circ \leq \theta_{\text{cm}} \leq 33.5^\circ$ ,  $17.01^\circ \leq \theta_{\text{cm}} \leq 10.9^\circ$  and  $6.3^\circ \leq \theta_{\text{cm}} \leq 3.5^\circ$  respectively. These data have also been divided into three centrality bins, (0 – 20)%, (30 – 50)% and (60 – 80)%, equivalent to  $0 \leq b \leq 3$  fm,  $4 \leq b \leq 5$  fm and  $5.5 \leq b \leq 6.3$  fm.

fm respectively. The results in the two lowest  $\eta$  bins are reported for  $(h^+ + h^-)/2$  while the  $\eta = 2.2$  and  $3.2$  bins are reported for  $h^-$  only where  $h^+$  and  $h^-$  stand for the positively and negatively charged hadrons respectively.

In this paper, we calculate  $R_{\text{dAu}}(p_T)$  in the BRAHMS  $\eta$  bins using two parameterizations of nuclear shadowing. We also calculate the central-to-peripheral ratios,  $R_{\text{CP}}(p_T)$ , with two parameterizations of the spatial dependence of shadowing. The calculated ratios are compared to the BRAHMS data [8]. To better illustrate the effects of shadowing alone, we do not include the Cronin effect,  $p_T$  broadening [9,10], in our calculations.

We make a leading order (LO) calculation of minijet production to obtain the yield of high- $p_T$  partons [11]. The  $p_T$  distribution of Ref. [12] is modified to include the nuclear parton distribution functions,

$$\frac{d\sigma_{\text{dAu} \rightarrow hX}}{d^2b dp_T} = 2p_T \sum_{i,j=q,\bar{q},g} \int_{\theta_{\min}}^{\theta_{\max}} \frac{d\theta_{\text{cm}}}{\sin \theta_{\text{cm}}} \int dx_1 \int dx_2 \int d^2s \int dz \int dz' \\ \times F_{i/\text{d}}(x_1, Q^2, \vec{s}, z) F_{j/\text{Au}}(x_2, Q^2, |\vec{b} - \vec{s}|, z') \frac{D_{h/k}(z_c, Q^2)}{z_c} \frac{d\hat{\sigma}_{ij \rightarrow k}}{d\hat{t}} \quad (3)$$

where  $x_1$  and  $x_2$  are the parton momentum fractions in the deuterium and gold nuclei respectively,  $Q$  is the momentum scale of the hard interaction and  $z_c$  is the fraction of the parton momentum transferred to the final-state hadron. The integrals over center-of-mass scattering angle,  $\theta_{\min} \leq \theta_{\text{cm}} \leq \theta_{\max}$ , correspond to the BRAHMS angular regions, given previously. The  $2 \rightarrow 2$  minijet cross sections,  $d\hat{\sigma}_{ij \rightarrow k}/d\hat{t}$ , are given in Ref. [13]. Even though the next-to-leading order corrections may affect the shape of the  $p_T$  distributions, the higher-order corrections should largely cancel out in  $R_{\text{dAu}}$ , as is the case for  $J/\psi$  [14] and Drell-Yan [11] production.

The parton densities in the gold nucleus,  $F_{j/\text{Au}}(x, Q^2, \vec{b}, z)$ , can be factorized into  $x$  and  $Q^2$  independent nuclear density distributions, position and nuclear-number independent nucleon parton densities, and a shadowing function,  $S_{\text{P,S}}^i(A, x, Q^2, \vec{b}, z)$ , that describes the modification of the nuclear parton distributions in position and momentum space. The first subscript on the shadowing function, P, refers to the shadowing parameterization while the second, S, to the spatial dependence. Most available shadowing parameterizations ignore

effects in deuterium so that  $F_{i/d}$  depends only on the deuterium density distribution and the nucleon parton densities. We account for the proton and neutron numbers of both nuclei. Then [14]

$$F_{i/d}(x, Q^2, \vec{s}, z) = \rho_d(\vec{s}, z) f_{i/N}(x, Q^2) \quad (4)$$

$$F_{j/Au}(x, Q^2, |\vec{b} - \vec{s}|, z') = \rho_{Au}(|\vec{b} - \vec{s}|, z') S_{P,S}^j(Au, x, Q^2, |\vec{b} - \vec{s}|, z') f_{j/N}(x, Q^2) \quad (5)$$

where  $f_{i/N}(x, Q^2)$  is the nucleon parton density. In the absence of nuclear modifications,  $S_{P,S}^j \equiv 1$ . The nucleon density distribution of the gold nucleus is assumed to be a Woods-Saxon with  $R_{Au} = 6.38$  fm [15]. We use the Hulthén wave function [16] to calculate the deuteron density distribution. The densities are normalized so that  $\int d^2s dz \rho_A(\vec{s}, z) = A$ . We use the MRST LO parton distributions [17] for isolated nucleons and take  $Q^2 = p_T^2$ .

We have chosen two parameterizations of nuclear shadowing which cover extremes of gluon shadowing at low  $x$ . The Eskola *et al.* parameterization, EKS98, is based on the GRV LO [18] parton densities. At the minimum scale,  $Q_0^2$ , valence quark shadowing is identical for  $u$  and  $d$  quarks. Likewise,  $\bar{u}$  and  $\bar{d}$  shadowing is identical at  $Q_0^2$ . Even though the light quark shadowing ratios are not constrained to be equal at higher scales, the differences between them are small. Shadowing of the heavier flavor sea,  $\bar{s}$  and higher, is calculated separately at  $Q_0^2$ . The shadowing ratios for each parton type are evolved to LO for  $2.25 < Q^2 < 10^4$  GeV and are valid for  $x \geq 10^{-6}$  [19,20]. Interpolation in nuclear mass number allows results to be obtained for any input  $A$ . The parameterization by Frankfurt, Guzey and Strikman, denoted FGS, combines Gribov theory with hard diffraction [21]. It is based on the CTEQ5M [22] parton densities and evolves each parton species separately to NLO for  $4 < Q^2 < 10^4$  GeV. Although the  $x$  range is  $10^{-5} < x < 0.95$ , the sea quark and gluon ratios are unity for  $x > 0.2$ . The EKS98 valence quark shadowing ratios are used as input since Gribov theory does not predict valence shadowing. The parameterization is available for four different values of  $A$ : 16, 40, 110 and 206. We use the  $A = 206$  parameterization for the gold nucleus.

We now turn to the spatial dependence of the shadowing. Since some qualitative spatial dependence has been observed [23] but the exact behavior is unknown, we use two different

parameterizations for inhomogeneous shadowing in d+Au collisions [11,24–26]. The first,  $S_{\text{P,WS}}$ , assumes that shadowing is proportional to the local density,  $\rho_A(r)$ ,

$$S_{\text{P,WS}}^j(A, x, Q^2, \vec{s}, z) = 1 + N_{\text{WS}}[S_{\text{P}}^j(A, x, Q^2) - 1] \frac{\rho_A(r)}{\rho_A(0)}, \quad (6)$$

where  $r = \sqrt{s^2 + z^2}$ ,  $\rho_A(0)$  is the central density and  $N_{\text{WS}}$  is chosen so that  $(1/A) \int d^2s dz \rho_A(\vec{s}, z) S_{\text{P,WS}}^j = S_{\text{P}}^j$ . When  $r \gg R_A$ , the nucleons behave as free particles while, at the center of the nucleus, the modifications are larger than  $S_{\text{P}}^j$ .

If, instead, shadowing stems from multiple interactions of the incident parton [27], parton-parton interactions are spread longitudinally over the coherence length,  $l_c = 1/2m_N x$ , where  $m_N$  is the nucleon mass [28]. For  $x < 0.016$ ,  $l_c > R_A$  for any  $A$  and the incident parton interacts coherently with all the target partons in its path so that

$$S_{\text{P},\rho}^j(A, x, Q^2, \vec{s}, z) = 1 + N_\rho[S_{\text{P}}^j(A, x, Q^2) - 1] \frac{\int dz \rho_A(\vec{s}, z)}{\int dz \rho_A(0, z)}. \quad (7)$$

The integral over  $z$  includes the material traversed by the incident nucleon. The normalization requires  $(1/A) \int d^2s dz \rho_A(\vec{s}, z) S_{\text{P},\rho}^j = S_{\text{P}}^j$  with  $N_\rho > N_{\text{WS}}$ . At large  $x$ ,  $l_c \ll R_A$  and shadowing is proportional to the local density, Eq. (6).

The fragmentation functions,  $D_{h/k}(z_c, Q^2)$ , are the probability for the production of hadron  $h$  from parton  $k$  with  $z_c = p_h/p_k$ . The produced partons are fragmented into charged pions, kaons and protons using the LO KKP fragmentation functions [29], fit to  $e^+e^-$  data. The final-state hadrons are assumed to be produced pairwise so that  $\pi \equiv (\pi^+ + \pi^-)/2$ ,  $K \equiv (K^+ + K^-)/2$ , and  $p \equiv (p + \bar{p})/2$ . The equality of  $p$  and  $\bar{p}$  production obviously does not describe low energy hadroproduction well. At higher energies, however, the approximation that  $p = \bar{p}$  may be more reasonable. The produced hadrons follow the parent parton direction. The minimum  $Q^2$  in the KKP fragmentation functions is  $Q_{\text{Fr0}}^2 = 2 \text{ GeV}^2$ , similar to but somewhat lower than the minimum  $Q^2$  of the shadowing parameterizations. Thus the minimum  $p_T$  of our calculations is  $\sqrt{2} \text{ GeV}$ . We assume the same scale in the parton densities and the fragmentation functions,  $Q^2 = Q_{\text{Fr}}^2 = p_T^2$ . A larger scale,  $p_T^2/z_c^2$ , is sometimes used in the parton densities but at high  $p_T$ , where  $z_c$  is large, as is the case here, changing the scale does not significantly alter the calculated ratios.

The largest contribution to the total final-state charged particle production is from the charged pions, followed by the kaons. The proton contribution is the smallest even though, in d+Au collisions at RHIC,  $(p + \bar{p})/h \approx 0.24 \pm 0.02$  where  $h = h^+ + h^-$  for  $2 < p_T < 3$  GeV, independent of centrality [30]. The d+Au result is similar to that from  $pp$ ,  $0.21 \pm 0.01$  [30]. The discrepancy between the RHIC d+Au and  $pp$  results and the extrapolation from  $e^+e^-$  is due to the poor knowledge of the fragmentation functions at large  $z_c$ .

We have calculated the  $p_T$  distributions for final-state charged pions, kaons and protons/antiprotons separately as well as the sum of all charged particles. For each final-state hadron, we determine the fraction of the total from produced quarks, antiquarks and gluons. In the central  $\eta$  bin for pion production, gluons are produced almost equally in the  $gg \rightarrow gg$  and  $qg \rightarrow qg$  channels. The  $qg$  channel is somewhat larger for  $p_T > 5$  GeV. There is a negligible contribution from  $q\bar{q} \rightarrow gg$ . Pion production by quarks and antiquarks proceeds mainly through the  $qg \rightarrow qg$  channel for quarks and  $\bar{q}g \rightarrow \bar{q}g$  for antiquarks. The next largest contribution to pion production by quarks are the  $qq' \rightarrow qq'$  and  $qq \rightarrow qq$  channels which are of very similar strength, followed by  $q\bar{q} \rightarrow q\bar{q}$  and  $gg \rightarrow q\bar{q}$  with a negligible contribution from  $q\bar{q} \rightarrow q'\bar{q}'$ . The contributions to antiquark production after  $\bar{q}g \rightarrow \bar{q}g$  are  $\bar{q}q' \rightarrow \bar{q}q'$ ,  $\bar{q}q \rightarrow \bar{q}q$  and  $gg \rightarrow q\bar{q}$ , followed by smaller contributions from  $\bar{q}q \rightarrow \bar{q}q$  and  $q\bar{q} \rightarrow q'\bar{q}'$ . Similar results are found for kaon and proton production. However, the proton distributions fall off more steeply with  $p_T$ .

The relative contributions from the production channels remains similar as rapidity increases. The most important change is in gluon production where the  $qg \rightarrow qg$  channel grows more dominant, finally becoming larger than the  $gg \rightarrow gg$  channel for all  $p_T$  for  $\eta = 3.2$ . Indeed, at the most forward rapidity, the  $q\bar{q} \rightarrow gg$  channel becomes comparable to the  $qg$  channel at  $p_T \sim 8$  GeV. This may seem counterintuitive since the ion  $x_2$  value decreases as  $\eta$  grows, increasing the gluon density. However, the deuteron  $x_1$  value increases more rapidly and, at large  $\eta$ , we are in a region where the deuteron gluon density is dropping steeply while the quark density, particularly that of the valence quarks, is still significant. Thus the  $qg$  channel is more important than the  $gg$  channel at large  $\eta$ , particularly when  $p_T$  and  $x_1$

are large. Also, at high  $\eta$  and  $p_T$ ,  $p_T > 7.5$  GeV, antiquarks are predominantly produced by valence quark induced processes, since these are large at high  $x$ .

Since we begin to approach the edge of phase space with increasing  $\eta$ , the  $p_T$  distributions steepen, especially for antiquark and gluon production. Quark production, which includes the valence contribution, dominant at high  $p_T$  and  $\eta$ , remains harder overall. Thus quark production will come to dominate all final-state hadron production. This effect, increasingly important at high  $p_T$  and  $\eta$ , is reflected in the relative contributions to pion, kaon and proton production by quarks, antiquarks and gluons. At  $|\eta| \leq 0.2$ , pion production is dominated by produced gluons up to  $p_T > 9$  GeV where pion production by quarks becomes larger. Gluon production of kaons is rather small, similar to the quark contribution at  $p_T \sim Q_{\text{Fr}_0}$  but dropping below the antiquark contribution at  $p_T \sim 3.5$  GeV. Quark production is most important for protons at  $p_T > 3.5$  GeV. As  $\eta$  increases, quark production of final-state hadrons becomes increasingly dominant. Already at  $\eta = 1$ , more than half of all kaons and protons are produced by quarks for  $p_T > 2.5$  GeV. At higher  $\eta$ , antiquarks and gluons make negligible contributions to low  $p_T$  kaon and proton production at  $\eta = 2.2$  and 3.2. Quarks also dominate pion production for  $p_T > 6.5, 3$  and 1.5 GeV with  $\eta = 1, 2.2$  and 3.2 respectively.

We have calculated the average Au ion momentum fraction,  $\langle x_2 \rangle$ , and the average deuteron momentum fraction,  $\langle x_1 \rangle$ , for  $\sqrt{2} \leq p_T \leq 12$  GeV. However, the largest accessible  $p_T$  decreases to 9.5 GeV for  $\eta = 3.2$  due to phase space. The results are shown in Table I. Since these are average  $x_2$  values, the actual  $x_2$  for each event can be smaller or larger than these averages. The minimum and maximum  $\langle x_2 \rangle$  correspond to the lowest and highest  $p_T$  values respectively. Both the minimum and maximum values decrease as  $\eta$  increases so that the minimum  $\langle x_2 \rangle$  is reached at  $\eta = 3.2$ . However, the maximum  $\langle x_2 \rangle$  increases relative to more central  $\eta$  values due to the reduction of phase space at high  $p_T$ . Note that as  $\theta \rightarrow 0$ ,  $\langle x_2 \rangle \rightarrow 1$ . The averages are not very sensitive to changes in the parton densities or the choice of factorization, renormalization or fragmentation scales.

The total hadron yield closely follows that of the pions. There is little variation of

$\langle x_2 \rangle$  between hadron species although the proton averages are generally somewhat smaller than those of the mesons. A small difference between the partonic contributions to hadron production can be attributed to the behavior of the parton distribution functions in the various production channels. A set of LO parton densities derived including the GLRMQ recombination terms at low  $x$  found deviations from normal DGLAP evolution at  $x < 10^{-3}$  for the proton [31]. Thus one may question whether saturation effects can be at work here, especially since  $\langle x_2 \rangle = 0.035$  at  $\eta = 3.2$ .

While the average Au momentum fraction is decreasing with centrality, the average deuteron momentum fraction,  $x_1$ , is increasing. Note that the maximum  $\langle x_1 \rangle$  at  $\eta = 3.2$  approaches 1, indicative of the edge of phase space. The average  $z_c$  in the fragmentation functions is large,  $\approx 0.5$  at midrapidity, and increasing with  $\eta$  and  $p_T$ . The fragmentation functions are best determined for smaller  $z_c$  so that the high  $z_c$  fragmentation functions are unreliable, especially for baryon production. Modeling of high  $p_T$  and high  $\eta$  hadron production thus contains large theoretical uncertainties due to the fragmentation functions. There is more variation in  $\langle z_c \rangle$  due to parton type than in  $\langle x_2 \rangle$ . The proton  $\langle z_c \rangle$  tends to be somewhat smaller than for pions or kaons. The tabulated values are for total charged hadrons.

We now compare the ratios,  $R_{dAu}$ , calculated for the two homogeneous shadowing parameterizations, to the BRAHMS data [8]. The EKS98 results are shown for each  $\eta$  interval in Fig. 1 while those employing the FGS parameterization are shown in Fig. 2. We show the results for charged pions (dashed), charged kaons (dot-dashed) and protons/antiprotons (dotted) separately. The solid curves give the total charged hadron result. At midrapidity, where  $\langle x_2 \rangle$  is relatively large, the two parameterizations give rather similar results. As pointed out in Ref. [32], the difference between the kaon and proton ratios is due to isospin effects. As long as pion production is dominated by gluons, it is essentially independent of isospin. The ratio is greater than unity but smaller than the BRAHMS result at midrapidity. Including  $p_T$  broadening would increase the  $|\eta| \leq 0.2$  ratio.

At  $\eta = 1$  and low  $p_T$ , the ratio is less than unity for both parameterizations but the

stronger gluon shadowing in the FGS parameterization reduces  $R_{\text{dAu}}$  to  $\sim 0.8$  for  $p_T = \sqrt{2}$  GeV relative to  $\sim 0.9$  for EKS98. At  $p_T \sim 2.5$  GeV,  $R_{\text{dAu}}$  rises above unity again. At higher rapidities,  $R_{\text{dAu}}$  decreases at low  $p_T$  but does not rise as far above unity at higher  $p_T$  until at  $\eta = 3.2$ , the total charged hadron ratio is less than unity for all  $p_T$ . The EKS98 parameterization tends to underestimate the data for all but the most central rapidities, see Fig. 1. The FGS parameterization, on the other hand, agrees rather well with the central  $\eta$  data, Fig. 2(a), and lies within the errors of the most peripheral bins for  $p_T > \sqrt{2}$  GeV, Fig. 2(c) and (d). However, the total charged hadron data at  $\eta = 1$  are somewhat underestimated by the FGS parameterization, Fig. 2(b).

In the most central bins, the ratio for the total charged hadrons closely follows  $R_{\text{dAu}}$  for the pions. At higher  $\eta$ , the kaon contribution becomes more important, causing the total to be closer to the average of the pion and kaon results. The proton contribution, on the other hand, remains small, even at  $\eta = 3.2$ , while one may expect that, in reality, proton production would be more important at large rapidity as the fragmentation region is approached. However, this effect cannot be accounted for by standard parameterizations of the fragmentation functions. Since BRAHMS measures the negative charged hadron distribution,  $h^-$ , at  $\eta = 2.2$  and  $3.2$ , only the antiprotons can contribute to  $R_{\text{dAu}}$ .

We point out that because  $x$  is not very small for  $p_T$  larger than a few GeV and the shadowing ratios are also not far from unity in this region,  $R_{\text{dAu}}$ , the ratios of d+Au relative to  $pp$  are driven by the isospin rather than shadowing. This is obvious from the very similar behavior of the EKS98 and FGS ratios seen in Figs. 1 and 2 for  $p_T > 5$  GeV.

Figures 3 and 4 illustrate the centrality dependence of the inhomogeneous shadowing results with the FGS parameterization. We compare the central-to-peripheral ratio,  $R_{\text{CP}}$ , which should be less sensitive to isospin than  $R_{\text{dAu}}$ , for the two inhomogeneous shadowing parameterizations,  $S_{\text{FGS,ws}}$  in Fig. 3 and  $S_{\text{FGS},\rho}$  in Fig. 4, to the BRAHMS data. The solid curves show the ratio of the central,  $(0 - 20)\%$ , to peripheral,  $(60 - 80)\%$ , bins for each  $\eta$  region while the dashed curves show the semi-central,  $(30 - 50)\%$ , to peripheral ratios. Our

calculations assume exact impact parameter cuts while, experimentally, impact parameter is poorly measured on an event-by-event basis.

In central collisions, with small impact parameter, inhomogeneous shadowing is stronger than the homogeneous result. The larger the homogeneous shadowing effect, the larger the difference between  $S_P$  and  $S_{P,S}$ . Thus  $R_{CP}$  is a stronger function of impact parameter for the FGS parameterization since it has larger homogeneous shadowing at small  $x$ . The ratios with  $S_{EKS,S}$  underestimate the centrality dependence considerably and are not shown. Note that  $R_{CP}$  approaches unity at large  $p_T$  since the difference between  $S_P$  and  $S_{P,S}$  decreases as  $x$  increases and the shadowing effect becomes small.

The impact parameter dependence is rather weak for  $S_{FGS,WS}$ , shown in Fig. 3, due to the slow variation of  $\rho_{Au}(r)$  with  $r$  for  $r < R_{Au}$ . On the other hand,  $S_{FGS,\rho}$  increases more smoothly with impact parameter so that the  $b$  dependence of  $R_{CP}$  is stronger. The fluctuations in  $R_{CP}$  for  $S_{FGS,\rho}$ , especially notable at central rapidity, are due to the discrete steps of  $T_{Au}(r)$  in the integration over the spatial coordinates. These fluctuations are absent for  $S_{FGS,WS}$  since  $\rho_{Au}(r)$  is a smooth function.

The agreement with the data is fair for  $S_{FGS,\rho}$  at central  $\eta$ , see Fig. 4(a) and (b). However, the increase in  $\langle x_2 \rangle$  with  $p_T$  results in the strong growth of  $R_{CP}$  with  $p_T$  at forward  $\eta$ . The resulting curvature of the calculated ratio is opposite that of the data. The magnitude of  $R_{CP}$  at low  $p_T$  is also underestimated. Since the position dependence of inhomogeneous shadowing is not well understood, the poorer agreement with the centrality-dependent data in Figs. 3 and 4 compared to the minimum bias results in Figs. 1 and 2 is not surprising. These data could be used to tune the position dependence of shadowing. In addition, the FGS calculation of leading-twist shadowing included some impact parameter dependence [21] but this dependence is so far not included in the parameterization.

In summary, we find that the suppression factor,  $R_{dAu}$ , calculated with leading-twist shadowing, especially employing the FGS parameterization, agrees moderately well with the BRAHMS data. These calculations imply that saturation effects may not play a dominant role in the forward region at RHIC, as suggested in other recent work [33,34]. Our

calculations show a stronger  $p_T$  dependence than that suggested by BRAHMS, likely due to insufficient data on the impact parameter dependence of nuclear shadowing.

We thank K.J. Eskola and V. Guzey for providing the shadowing routines and S. R. Klein, M. Murray, M. Strikman and W. Vogelsang for discussions. This work was supported in part by the Division of Nuclear Physics of the Office of High Energy and Nuclear Physics of the U. S. Department of Energy under Contract Number DE-AC03-76SF0098.

## REFERENCES

- [1] K. Adcox *et al.* [PHENIX Collaboration], Phys. Lett. B **561**, 82 (2003) [arXiv:nucl-ex/0207009]; Phys. Rev. Lett. **88**, 022301 (2002) [arXiv:nucl-ex/0109003].
- [2] S. S. Adler *et al.* [PHENIX Collaboration], Phys. Rev. Lett. **91**, 072301 (2003) [arXiv:nucl-ex/0304022]; Phys. Rev. C **69**, 034910 (2004) [arXiv:nucl-ex/0308006].
- [3] C. Adler *et al.* [STAR Collaboration], Phys. Rev. Lett. **89**, 202301 (2002) [arXiv:nucl-ex/0206011].
- [4] J. Adams *et al.* [STAR Collaboration], Phys. Rev. Lett. **91**, 172302 (2003) [arXiv:nucl-ex/0305015].
- [5] I. Arsene *et al.* [BRAHMS Collaboration], Phys. Rev. Lett. **91**, 072305 (2003) [arXiv:nucl-ex/0307003].
- [6] S. S. Adler *et al.* [PHENIX Collaboration], Phys. Rev. Lett. **91**, 072303 (2003) [arXiv:nucl-ex/0306021].
- [7] J. Adams *et al.* [STAR Collaboration], Phys. Rev. Lett. **91**, 072304 (2003) [arXiv:nucl-ex/0306024].
- [8] I. Arsene *et al.* [BRAHMS Collaboration], arXiv:nucl-ex/0403005.
- [9] M. Gyulassy, P. Lévai and I. Vitev, Phys. Lett. B **538**, 282 (2002) [arXiv:nucl-th/0112071].
- [10] I. Vitev, M. Gyulassy and P. Lévai, Acta Phys. Hung. New Ser. Heavy Ion Phys. **17**, 237 (2003) [arXiv:nucl-th/0204019].
- [11] V. Emel'yanov, A. Khodinov, S. R. Klein and R. Vogt, Phys. Rev. C **61**, 044904 (2000) [arXiv:hep-ph/9909427].
- [12] R. D. Field, *Applications Of Perturbative QCD* (Addison-Wesley, Redwood City, CA, 1989).

- [13] J. F. Owens, Rev. Mod. Phys. **59**, 465 (1987).
- [14] S. R. Klein and R. Vogt, Phys. Rev. Lett. **91**, 142301 (2003) [arXiv:nucl-th/0305046].
- [15] C. W. De Jager, H. De Vries and C. De Vries, Atom. Data Nucl. Data Tabl. **14** (1974) 479.
- [16] D. Kharzeev, E.M. Levin and M. Nardi, Nucl. Phys. A **730**, 448 (2004) [arXiv:hep-ph/0212316]; L. Hulthen and M. Sagawara, in *Handbuch der Physik*, **39** (1957).
- [17] A. D. Martin, R. G. Roberts, W. J. Stirling and R. S. Thorne, Phys. Lett. B **443**, 301 (1998) [arXiv:hep-ph/9808371].
- [18] M. Gluck, E. Reya and A. Vogt, Z. Phys. C **53**, 127 (1992).
- [19] K. J. Eskola, V. J. Kolhinen and P. V. Ruuskanen, Nucl. Phys. B **535**, 351 (1998) [arXiv:hep-ph/9802350].
- [20] K. J. Eskola, V. J. Kolhinen and C. A. Salgado, Eur. Phys. J. C **9**, 61 (1999) [arXiv:hep-ph/9807297].
- [21] L. Frankfurt, V. Guzey and M. Strikman, arXiv:hep-ph/0303022.
- [22] H. L. Lai *et al.* [CTEQ Collaboration], Eur. Phys. J. C **12**, 375 (2000) [arXiv:hep-ph/9903282].
- [23] T. Kitagaki *et al.*, Phys. Lett. B **214**, 281 (1988).
- [24] V. Emel'yanov, A. Khodinov, S. R. Klein and R. Vogt, Phys. Rev. C **56**, 2726 (1997) [arXiv:nucl-th/9706085].
- [25] V. Emel'yanov, A. Khodinov, S. R. Klein and R. Vogt, Phys. Rev. Lett. **81**, 1801 (1998) [arXiv:nucl-th/9805027].
- [26] V. Emel'yanov, A. Khodinov, S. R. Klein and R. Vogt, Phys. Rev. C **59**, R1860 (1999) [arXiv:hep-ph/9809222].

- [27] A. L. Ayala, M. B. Gay Ducati and E. M. Levin, Nucl. Phys. B **493**, 305 (1997) [arXiv:hep-ph/9604383].
- [28] Z. Huang, H. Jung Lu and I. Sarcevic, Nucl. Phys. A **637**, 79 (1998) [arXiv:hep-ph/9705250].
- [29] B. A. Kniehl, G. Kramer and B. Pötter, Nucl. Phys. B **582**, 514 (2000) [arXiv:hep-ph/0010289].
- [30] J. Adams *et al.* [STAR Collaboration], arXiv:nucl-ex/0309012.
- [31] K. J. Eskola, H. Honkanen, V. J. Kolhinen, J. w. Qiu and C. A. Salgado, Nucl. Phys. B **660**, 211 (2003) [arXiv:hep-ph/0211239].
- [32] S. R. Klein and R. Vogt, Phys. Rev. C **67**, 047901 (2003) [arXiv:nucl-th/0211066].
- [33] J. Jalilian-Marian, arXiv:hep-ph/0402080.
- [34] D. Kharzeev, Yu. V. Kovchegov and K. Tuchin, arXiv:hep-ph/0405045.

## TABLES

$\langle\eta\rangle$	$\langle x_2 \rangle$		$\langle x_1 \rangle$		$\langle z_c \rangle$	
	min	max	min	max	min	max
$\approx 0$	0.07	0.22	0.07	0.22	0.52	0.64
1	0.055	0.18	0.1	0.33	0.54	0.68
2.2	0.042	0.14	0.17	0.62	0.55	0.81
3.2	0.035	0.23	0.32	0.95	0.64	0.96

TABLE I. The average values of the Au and d momentum fractions,  $\langle x_2 \rangle$  and  $\langle x_1 \rangle$  respectively, as well as the average fraction of the final-state parton momentum transferred to the hadron,  $\langle z_c \rangle$ , in the four BRAHMS pseudorapidity intervals. The minimum values correspond to  $p_T \approx \sqrt{2}$  GeV while the maximum corresponds to  $p_T = 12$  GeV for the first three  $\eta$  bins and 10 GeV for the most forward  $\eta$  bin.

## FIGURES

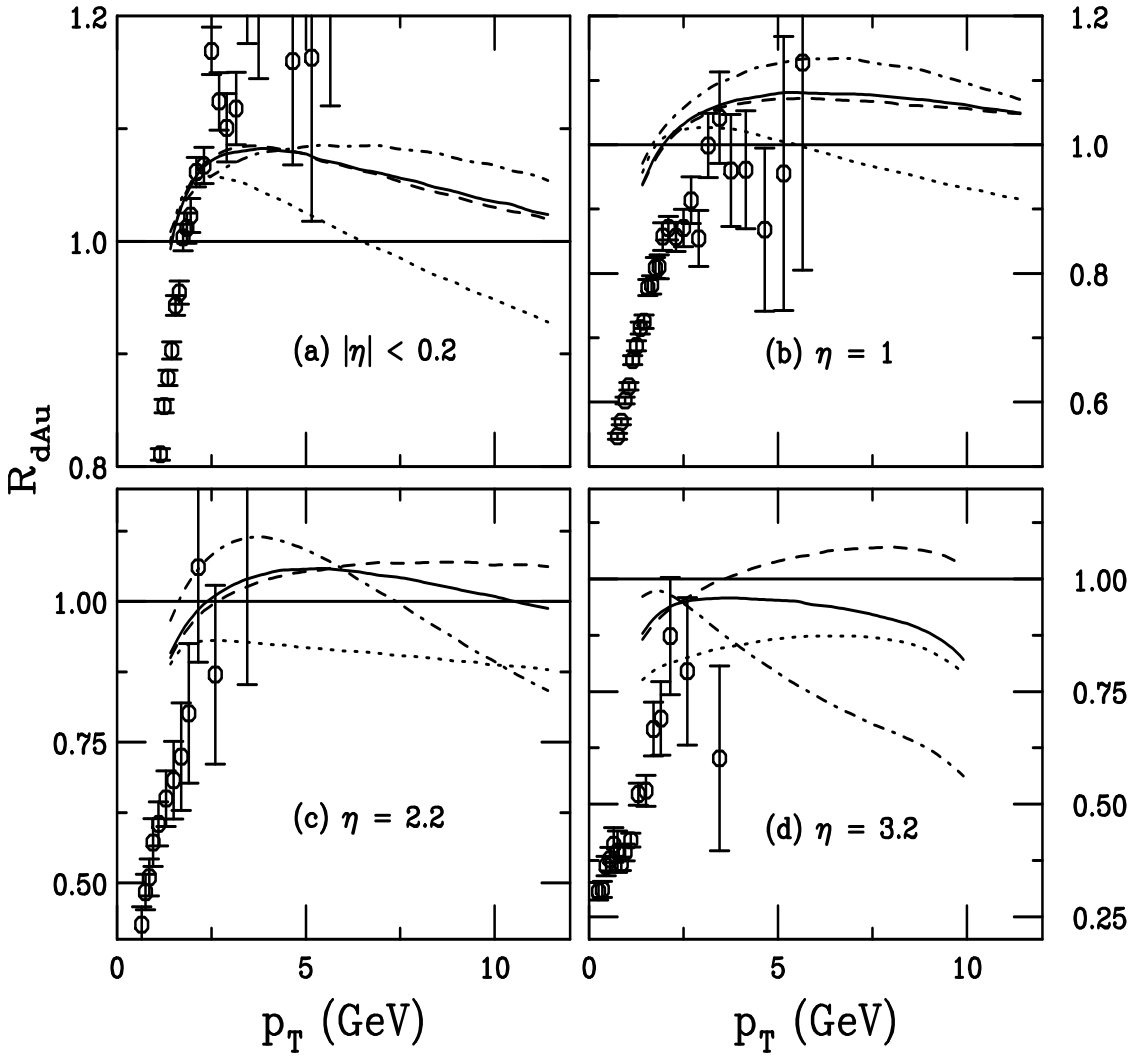


FIG. 1.  $R_{dAu}$  for charged pions (dashed) and kaons (dot-dashed) as well as protons and antiprotons (dotted) and the sum over all charged hadrons (solid) for deuteron-gold collisions at  $\sqrt{S_{NN}} = 200$  GeV as a function of  $p_T$ . The results for homogeneous shadowing with the EKS98 parameterization are compared to the BRAHMS data [8] in the following  $\eta$  bins: (a)  $|\eta| \leq 0.2$ ; (b)  $\eta = 1$ ; (c)  $\eta = 2.2$  and (d)  $\eta = 3.2$ .

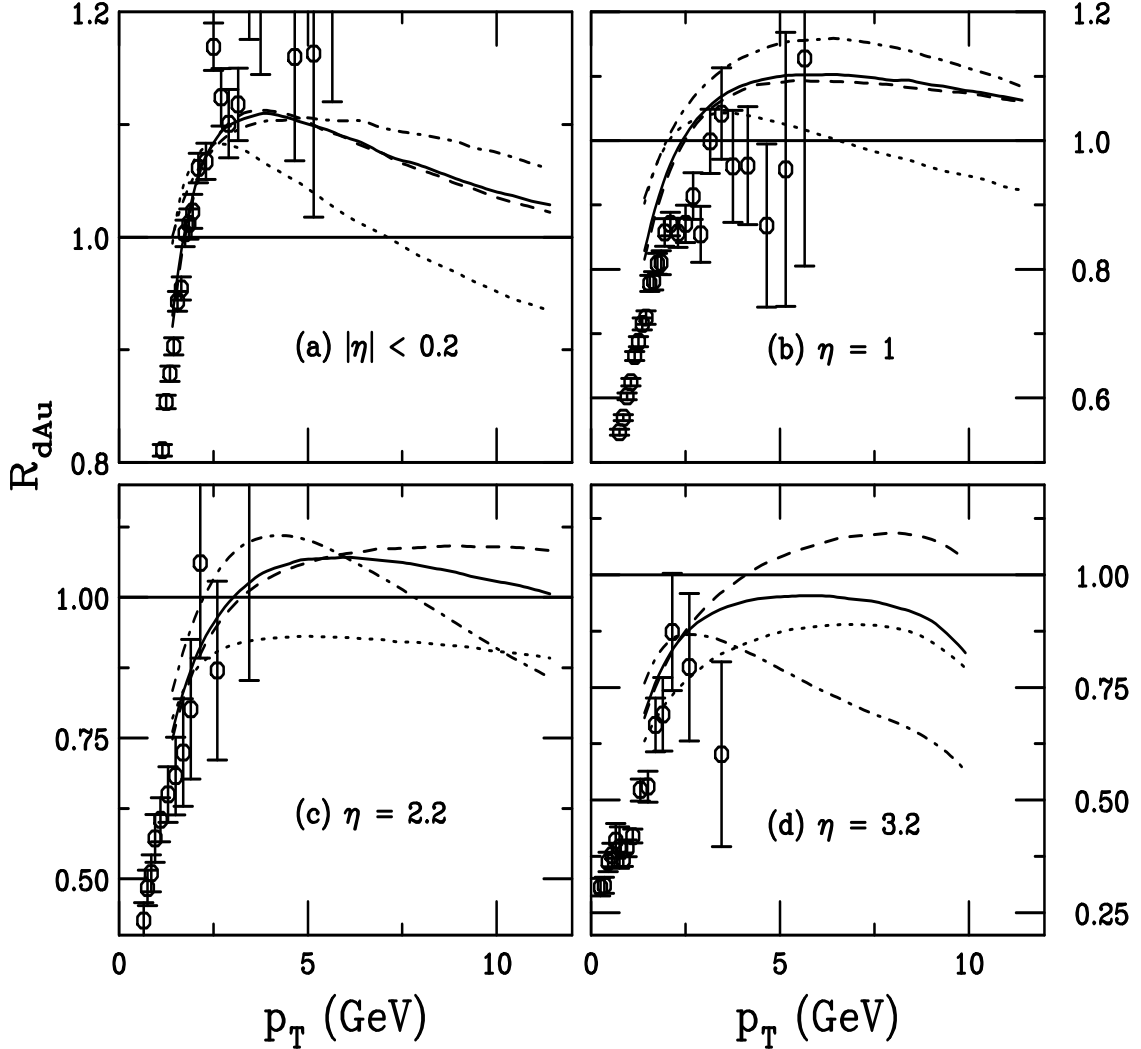


FIG. 2.  $R_{dAu}$  for charged pions (dashed) and kaons (dot-dashed) as well as protons and antiprotons (dotted) and the sum over all charged hadrons (solid) for deuteron-gold collisions at  $\sqrt{S_{NN}} = 200$  GeV as a function of  $p_T$ . The results for homogeneous shadowing with the FGS parameterization are compared to the BRAHMS data [8] in the following  $\eta$  bins: (a)  $|\eta| \leq 0.2$ ; (b)  $\eta = 1$ ; (c)  $\eta = 2.2$  and (d)  $\eta = 3.2$ .

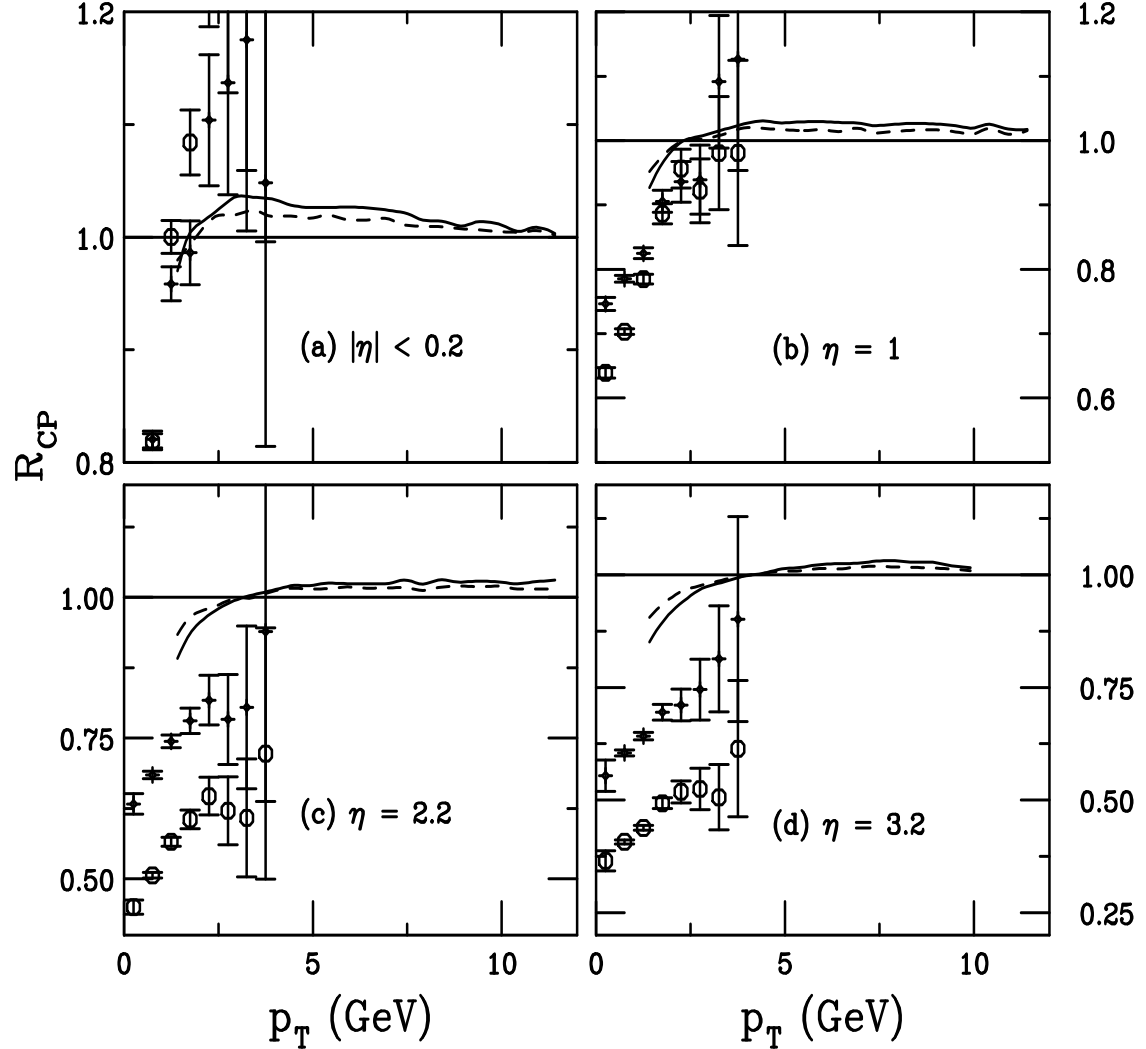


FIG. 3.  $R_{CP}$  for charged hadrons in deuteron-gold collisions at  $\sqrt{S_{NN}} = 200$  GeV as a function of  $p_T$ . The results for  $S_{FGS,WS}$  are compared to the BRAHMS data [8] in the following  $\eta$  bins: (a)  $|\eta| \leq 0.2$ ; (b)  $\eta = 1$ ; (c)  $\eta = 2.2$  and (d)  $\eta = 3.2$ . The calculated ratios of the most central and semi-central to peripheral collisions are shown in the solid and dashed curves, respectively. The BRAHMS data are given by the open circles (most central) and diamonds (semi-central).

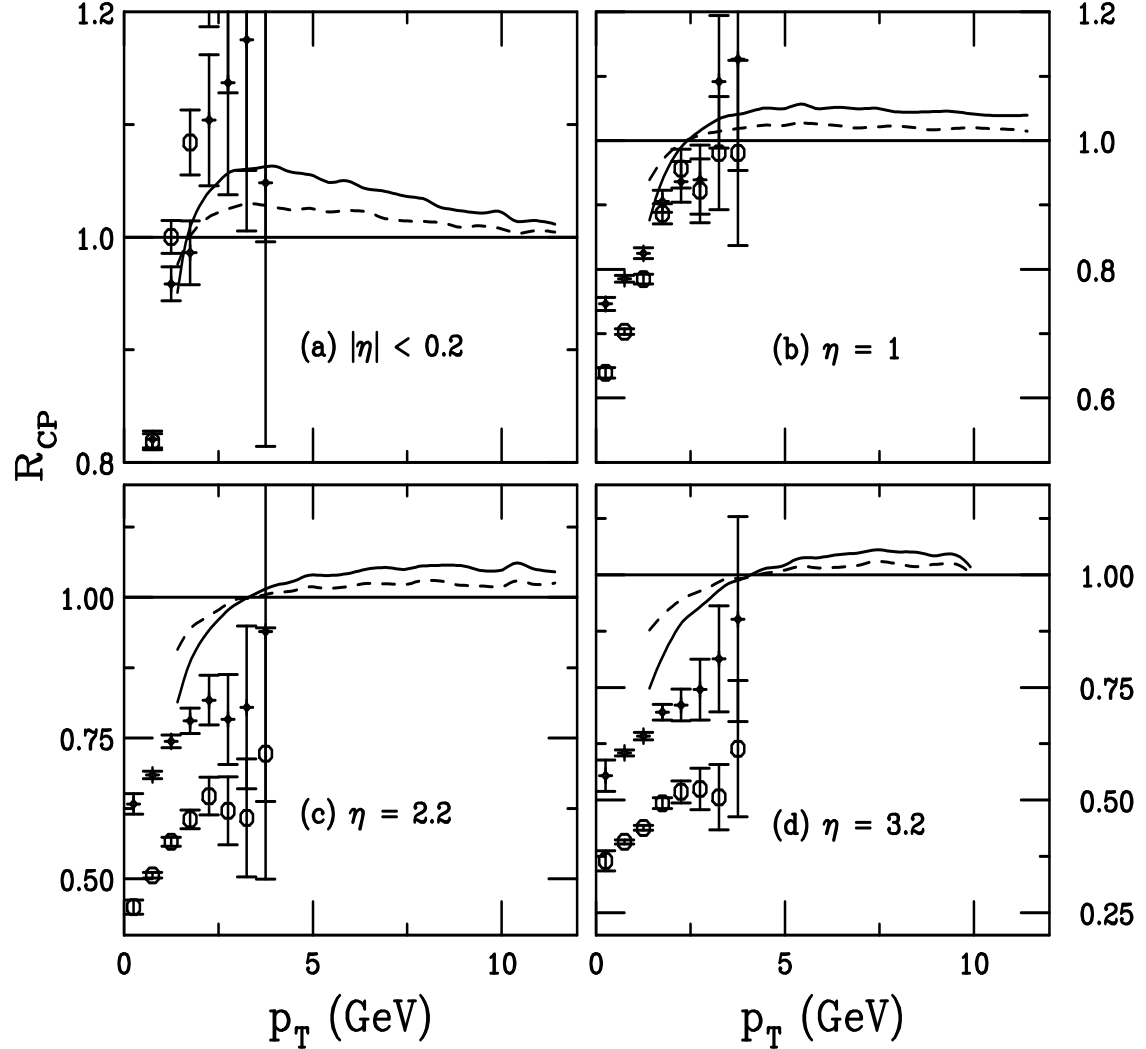


FIG. 4.  $R_{CP}$  for charged hadrons in deuteron-gold collisions at  $\sqrt{S_{NN}} = 200$  GeV as a function of  $p_T$ . The results for  $S_{FGS,\rho}$  are compared to the BRAHMS data [8] in the following  $\eta$  bins: (a)  $|\eta| \leq 0.2$ ; (b)  $\eta = 1$ ; (c)  $\eta = 2.2$  and (d)  $\eta = 3.2$ . The calculated ratios of the most central and semi-central to peripheral collisions are shown in the solid and dashed curves, respectively. The BRAHMS data are given by the open circles (most central) and diamonds (semi-central).